Interface Shear Failure Behavior Between Normal Concrete (NC) and Ultra-High Performance Concrete (UHPC)

Boshan Zhang[1] , Jiangjiang Yu[2], Weizhen Chen[1], Jianbo Chen[3], Heng Li[2] and Jialun Niu[4*]

Abstract

Ultra-high performance concrete (UHPC) with excellent mechanical properties and durability is a promising material for reinforcement of existing normal concrete (NC) structures. In this paper, the shear failure behavior of the NC–UHPC interface was studied by the slant shear test and the SEM (scanning electron microscope) visualization test, considering influence of the substrate strength and the interface roughed treatment. As the NC substrate and the UHPC overlay are tightly combined at the interface transition zone (ITZ), the interface exhibits good slant shear performance, and the measured interfacial shear strength could reach 19.4 MPa with C40 substrate and 21.8 MPa with C50 substrate. In addition, the microstructure and composition of the ITZ, the possible interfacial failure modes, and the load-carrying mechanism of the interface under compression–shear force are revealed. The high interface roughness and the substrate strength have positive influence on the shear strength, and greatly affect the prone failure mode and the load-slip characteristic.

Keywords NC–UHPC interface, Interfacial shear failure, Interface roughness, Microstructure of ITZ (interface transition zone)

1 Introduction

Normal concrete (NC) is widely used due to the advantages of easily accessible raw materials, low cost, simple production process, and high adaptability. With the growing service time, damage occurs in existing concrete structures, and reinforcement is required when the design requirements could not be satisfied (Huang

*Correspondence:
Jialun Niu
niujialun@tongji.edu.cn
[1] Department of Bridge Engineering, Tongji University, Shanghai 200092, China
[2] Department of Building and Real Estate, Hong Kong Polytechnic University, Hong Kong 100872, China
[3] Highway Development Center of Hekou District, Dongying 257200, China
[4] Department of Geotechnical Engineering, Tongji University, Shanghai 200092, China

et al., 2022; Zhang et al., 2022). The section enlargement method is one of the most widely used reinforcement methods for concrete structures, in which the interfacial performance between the repair material layer and the existing concrete structure is a key factor affecting the repair effects (Paschalis & Lampropoulos, 2021). Ultra-high performance concrete (UHPC) is one of the promising repair materials as it has extremely high mechanical properties and durability, resulting in reduced outer layer thickness and excellent energy consumption performance (Yu et al., 2020, 2022a).

The interface performance between NC and UHPC is affected by various factors, such as surface treatment methods, moisture conditions, pouring methods, and aggregate grading (Ekaputri et al., 2022). Many studies have been conducted in this field. Zhang et al. (2020) investigated the effects of various factors, including the substrate surface roughness, the UHPC aging degree, the substrate moisture content, the UHPC setting time, the

Zhang *et al. Int J Concr Struct Mater*   (2024) 18:18

Page 2 of 16

substrate strength, the adhesive and expansion agents on the bonding strength. It demonstrated that the surface roughness and moisture degree of the substrate and the NC strength are the major factors, and the interfacial strength is close to or even exceeds that of NC. Harris et al. (2014) analyzed the bonding performance between UHPC and NC by experimental and numerical analysis, and tried to quantitatively characterize the substrate surface roughness parameters. The results proved the exceptional performance of the bond performance between NC and UHPC in the absence of bonding agents. Carbonell et al. (2014) conducted a series of research on the effect of surface roughness, the water content of the substrate concrete, UHPC age, and freeze–thaw cycle on the repair of ordinary concrete by UHPC. The results show that UHPC can provide sufficient bonding strength for the interface. Jafarinejad et al. (2019) prepared different substrate surfaces by grooving, wire brushing, casting, and sandblasting. Compared with the sample without surface treatment, the bond strength of the rough interface prepared by sandblasting increased by 4 times. Hallaq et al. (2017) prefabricated different surface conditions of NC substrates by wire brushing, drilling, and sandblasting method. The results indicate that compared with the casting interface surface (i.e., without any surface treatment), the sandblasting surface treatment can improve the bond strength by 2.5 times. Feng et al. (2022) investigated the microstructure of the interface transition zone (ITZ) and the interface bonding mechanism. Compared to the NC–NC interface, the NC–UHPC interface gains better bond strength due to the more compact and thinner ITZ where the number and width of cracks and gaps significantly reduce. Although these studies have put great efforts on the interfacial bonding properties between the UHPC layer and the NC substrate, there was no unified evaluation on the interfacial bonding properties of NC–UHPC composites prepared by different surface treatment methods. Ignoring the investigation of interface roughness may lead to inaccurate calculation results.

Experimental methods are widely adopted to test the bond performance between the old and the new concrete material layers, and the common methods include the direct shear test (Feng et al., 2020), the bi-surface shear test (Valikhani et al., 2020), the push-out test (Yang et al., 2022), and the slant shear test (Bentz et al., 2018; Hu et al., 2020). Zanotti et al. () investigated the effect of different types of fiber and concrete strength on bond performance using the slant shear test. The results indicate that the increase of interfacial cohesion due to fiber reinforcement is due to the increase of friction, while the increase of substrate strength leads to stronger interfacial adhesion due to the denser microstructure. Carbonell

et al. (2014) studied the bonding characteristics between UHPC and NC under different stress configurations and different freeze–thaw cycle conditions using the slant shear test, the splitting tensile, and pull-out test methods. The slant shear tests were carried out at different interface angles, and the bond properties under the different combinations of compressive stress and shear stress were analyzed more widely. Aaleti et al. (2019) evaluated the influence of shear friction parameters, the concrete strength, and the interface roughness on interface bonding performance through the slant shear test. It was found that the bonding performance between NC and UHPC largely depends on interface roughness. A minimum roughness of 1.6 mm is sufficient to develop a satisfactory bond strength between the UHPC and NC interfaces. Feng et al. (2020) evaluated the bonding properties of NC and UHPC by slant shear test and splitting tensile strength test with different inclination angles. The Mohr–Coulomb criterion was used to calculate the interfacial bond strength and internal friction with three different angles and evaluate the difference between the different repair materials. In practical engineering, the bond between an existing structure and the repair material layer is usually under the shear compression composite stress state. The effect of shear friction on the interfacial debonding behavior should be considered, and the slant shear test is could evaluate the bond strength under this stress state. However, most of the studies on the interfacial friction and slip characteristics have not been well demonstrated, and the contribution of this shear friction to the bonding performance has not been well-described.

In this paper, the interfacial friction, slip characteristics, and enhancement mechanism of NC–UHPC composite samples were investigated considering different substrate strength and interfacial roughness configurations. Based on the experimental results of a series of slant shear tests and microstructure scanning tests of the ITZ, the debonding failure modes, the bearing capacity, and the interface slip characteristics were investigated, and the bond failure mechanism was revealed. This work will provide a reference for the interface design and practical application of damaged NC structures strengthened by UHPC.

2 Experimental Program
2.1 Materials Information
In this research NC with C40 and C50 grade was used for the substrate, and UHPC was used for the overlay. The mix proportions and the tested compressive strength at the age of 28 days are given in Table 1.

The powder raw materials of NC are the P.O. 42.5R ordinary Portland cement and the fly ash. The natural

Zhang *et al. Int J Concr Struct Mater*   (2024) 18:18

Page 3 of 16

Table 1 Mix proportions and compressive strength of NC and UHPC

Raw materials	C40/C50 NC (kg/m³)		UHPC (kg/m³)	
Powder	Cement (42.5R) Fly ash	350.0/420.0 95.0/90.0	Cement (52.5R)	680.0
			Silica fume	81.6
			Quartz flour	272.0
Water		175.0/170.0		159.8
Superplasticizer		7.1/8.2		17.0
Fine aggregate	River sand (0–4.75 mm)	750.0/680.0	Quartz sand (0.15–0.20 mm)	169.8
			Quartz sand (0.25–0.60 mm)	433.6
Coarse aggregate	Broken basalt (4.75–19 mm)	1040.0/1060.0	Broken basalt (3–5 mm)	581.0
Fiber	–		Steel fiber	117.0
Compressive Strength	C40: 45.7 MPa C50: 56.1 MPa		135.5 MPa	

river sand and the crushed basalt were taken as the fine aggregate and the coarse aggregate, respectively. Besides water, the liquid superplasticizer was added to increase further the workability. The particle size of the sand and the basalt is 0–4.75 mm and 4.75–19 mm, respectively. The compressive strength tested by 150 mm cubic samples at 28 days is 45.7 MPa for C40 concrete and 56.1 MPa for C50 concrete.

For UHPC, the powder raw materials include the P.II. 52.5R cement as well as the superfine powder of silica fume and the quartz powder. The liquid materials include water and the superplasticizer. The quartz sand with the particle size of 0.15–0.20 mm and 0.25–0.60 mm was used as the fine aggregates, and the basalt with the particle size of 3–5 mm was used as the coarse aggregate. In addition, the copper-plated straight steel fiber with the length of 13 mm and the diameter of 0.2 mm was

applied with the volume fraction of 2%. Give the credit to its super tensile strength over 2850 MPa, the addition of fibers would significantly improve the toughness and the tensile strength of UHPC. The compressive strength tested by 100 mm cubic samples is 135.5 MPa.

2.2 Interface Treatment
Totally six interface treatment techniques were adopted in this research to treat the surface of the NC substrate and gain different roughed interface, as seen in Fig. 1. Among them, three methods, the slight roughing (SR, Fig. 1a), the heavy roughing (HR, Fig. 1b), and the prick roughing (PR, Fig. 1c), were prepared immediately after the initial setting of NC. The SR interface was formed by a serrated roughening blade with the tooth pitch of 5 mm and the tooth depth of 3 mm. The HR interface was formed by a ϕ10 ribbed bar with the target notch spacing

(a) SR	(b) HR	(c) PR	(d) CR-C2	(e) CR-C4	(f) CR-C6
R_q=0.41 mm	R_q=1.31 mm	R_q=0.91 mm	R_q=0.66 mm	R_q=0.47 mm	R_q=0.95 mm
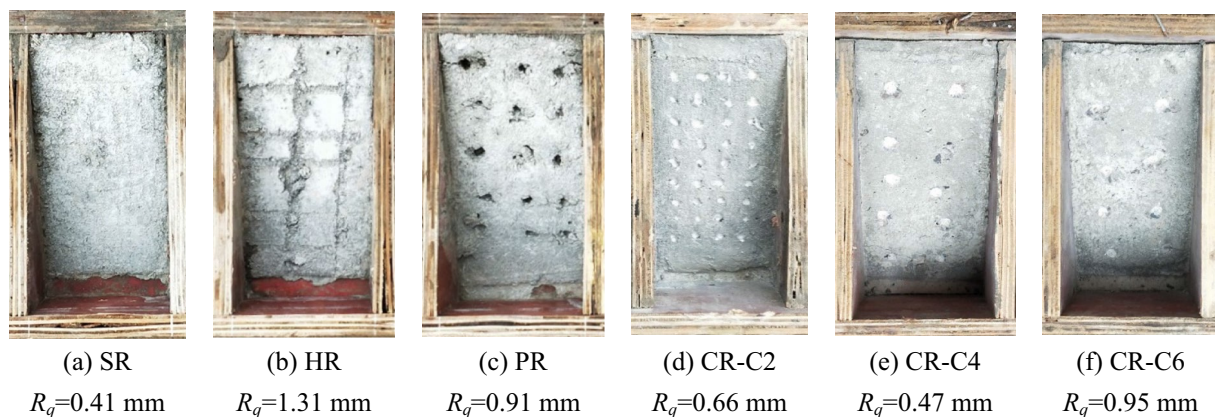
Fig. 1 Different kinds of RoughED surfaces

Zhang *et al. Int J Concr Struct Mater*   (2024) 18:18

Page 4 of 16

of 35 mm and notching depth of 3 mm. For the PR interface the hole spacing is around 30 mm and the hole depth is around 8 mm. While the other three chiseling roughing (CR) methods were carried out after 28-day curing of the NC part. For the surface marked as C2 (Fig. 1d), C4 (Fig. 1d), and C6 (Fig. 1f), the chiseling spacing is about 2 cm, 4 cm, and 6 cm respectively, and the chiseling depth is 3 mm, 4 mm, and 5 mm.

Each treated surface was scanned and measured by the 3D digital microscope, and the parameter, the root mean square roughness R_q, was adopted to characterize the roughness,

$$R_q = \sqrt{\frac{1}{A} \iint_A z^2(x, y) \mathrm{d}x\mathrm{d}y}, \tag{1}$$

where A is the area of the measured surface, $z(x, y)$ is the values of peaks and valleys measured from the average plane. The value of R_q is 0.41 mm for surface marked as SR, 1.31 mm for surface marked as HR, 0.91 mm for surface marked as PR, 0.66 mm for surface marked as C2, 0.47 mm for surface marked as C4, and 0.95mm for surface marked as C9.

2.3 Test Setup

2.3.1 Slant Shear Test

To explore the bond performance between NC and UHPC under shear and compression, the slant shear test was conducted on the NC–UHPC composite prism specimens as shown in Fig. 2a, where six kinds of roughed surface and two substrate strength grades were considered. The loading force is vertically applied to the top surface of the prism sample. To ensure the reliable contact between the loading equipment and the tested sample, pre-loading with the target force of 20 kN was conducted in advance, which is force-controlled with by 2 kN/s.

After that, the loading was applied at the rate of 0.1 mm/s until failure of the sample. Besides the force value, two linear variable differential transformers (LVDTs) were arranged vertically to record the loading displacement, and another two LVDTs were arranged along the interface on both sides to record the slip. The data were recorded synchronously during the loading process.

As shown in Fig. 2b, the $100 \times 100 \times 200$ mm prism sample consists two equal sections. Each section has a diagonally cast bonding area at a 30° angle from vertical. The NC part was first casted and cured for 28 days under standard curing. After that the UHPC part was casted and then the specimen was cured for another 28 days under the same condition.

2.3.2 Interface SEM Test

The structure and composition of the NC–UHPC interface on meso- and micro-scales were investigated by the SEM (scanning electron microscope) test. The tested samples shown in Fig. 3 were prepared as following process. First, the interface local small samples (less

Fig. 3 Samples of the SEM test

(a) test layout.

(b) dimensions of the slant shear specimen.

Fig. 2 Layout of NC–UHPC slant shear test (Unit: mm)

Zhang *et al. Int J Concr Struct Mater*   (2024) 18:18

Page 5 of 16

than 5 mm in dimension) were cut and separated from the specimen without mechanical testing. Then, these samples were kept in a sealed glass bottle and soaked in ethanol to prevent the cement from further hydration. Before the SEM test, the samples were taken out and dried. After that, these samples were placed in the epoxy resin gel with a vacuum environment for 0.5 h and then kept at room temperature for 24 h. Finally, the surface of the samples was leveled and polished with an automatic grinder, which was then coated with the conductive metal powder and fixed on the stage for the SEM test.

3 Results and Discussion

3.1 Bond Failure Mode

The failure modes of the slant shear samples can be divided into three categories according to the appearance of the damaged samples. They are mode (a) interface debonding failure, mode (b) interface debonding accompanied with substrate cracking, and mode (c) interface failure accompanied with crushed substrate. The typical samples for each failure mode are presented in Fig. 4. The variety of the failure mode lies in the friction constraint between the specimen and the loading planes, affecting the compressive properties of the concrete greatly. During the loading process, there will be frictional constraints between the upper and bottom planes of the slant shear specimen and the testing equipment. Before failure, this contact face friction belongs to the static friction, and the effect is basically linearly related to the load magnitude. When the load increases, the corresponding frictional constraint effect also increases. Thus, low interfacial bonding strength corresponds to low friction constraint effect between the sample and the loading equipment, resulting in little effect on the failure of the sample. The failure mode (a) occurs at the bonding interface as seen in Fig. 4a. On the contrary, samples with high interfacial bonding strength are faced with high friction constraint effect, which greatly affects the failure mode. The high constraint effect arises increasing number of diagonal cracks in the triangular area of the NC part near the contact plane. What's more, in the absence condition of any lubricant, the friction constraint effect will be significant. The shear expansion leads to the increase of slant cracks in the compression specimen, which causes the inverted cone failure mode of the prismatic specimen (Zhang et al., 2019). For the NC–UHPC slant shear specimen, because of the high strength performance of UHPC, almost all the specimens have no significant macro-cracks on the UHPC side.

According to the statistics, the failure modes for specimens with C40 substrate account for 22%, 22%, and 54% respectively for the mode (a), (b), and (c). While the value for specimens with C50 substrate is 50%, 17%, and 33%, respectively. It can be seen that most of the failure modes of slant shear specimens with low strength (C40) substrate are concentrated in the failure mode (c) of "interface failure + crushed substrate". However, in the case of C50 substrate strength, the failure mode (a) of "interface debonding" occurs in half of the slant shear specimens. The reason for this failure proportion distribution is that the slant shear specimen with low substrate NC strength has a weak ability to withstand compression, shear, and expansion. When the interface roughness between NC and UHPC is large, the bond effect is strong, and the compression load will cause the shear expansion cracks in the substrate NC part. As the loading process continues, the cracks in the interface and NC develop at the same time, and finally, the failure form of partial or complete debonding of the interface + NC substrate fragmentation occurs. For the specimen with C50 substrate strength, the resistance to shear expansion becomes stronger, so the number of specimens with the third failure mode decreases, and most of the samples showed the interfacial debonding failure mode.
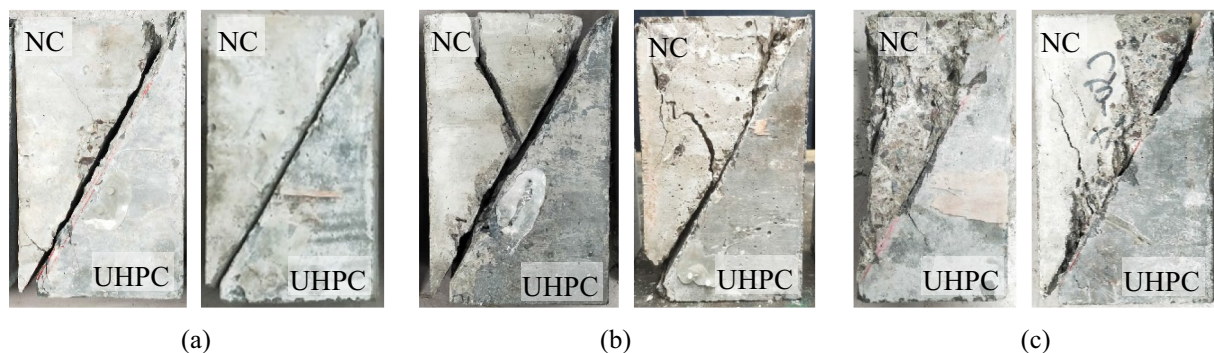

Fig. 4 Typical failure modes of the slant shear test: **a** interface debonding failure, **b** interface debonding + substrate cracking failure, **c** interface failure + substrate crushing failure

Zhang *et al. Int J Concr Struct Mater*   (2024) 18:18

Page 6 of 16

3.2 Bearing Capacity and Shear Resistance Contribution

The average load–displacement curve of the NC–UHPC slant shear test under different interface roughness configurations is shown in Fig. 5. It could be observed that the trend of the curves are similar. The curves grow linearly before occurrence of the failure. When approaching the ultimate load value, the micro-cracks rapidly expand near the interface or inside the NC substrate, and some load–displacement curves show small fluctuations similar to the "yielding" phenomenon, then the rapid reduction of load happens immediately and displays the brittle failure, while the displacement does not change. The reason for some load–displacement curves fluctuating before reaching the peak load is that when the stress is close to the interface shear failure value, some area of the NC substrate undergoes shear failure, which causes stress fluctuation consequently. However, this fluctuation is not enough to cause the total failure of the specimen, which can continue to bear the external load. Then, as the bonding action fails, the interface slip subsequently causes the sudden failure of the composite specimen. From the mechanism analysis of shear force transmission, it can be indicated that the shear bearing capacity of the interface is the balanced result between the bond action of friction sliding resistance and the micro-crack expansion process. The difference in the interface microstructure is shown by the difference in the shape and number of the outline protrusions, which will cause the difference in the interface shear resistance and further affect the macroscopic characteristics of the load–displacement curve.

Table 2 summarizes the bearing capacity of the tested slant shear samples, which is recognized as the peak value of the load–displacement curve. The relatively large dispersion reflects the inevitable differences in the manually processed interfaces. Then, the relationship between the bearing capacity and the roughness is plotted and fitted as seen in Fig. 6. The results indicate that the shear strength of NC–UHPC increases with the increase of roughness. On one hand, the increase in roughness will cause the undulation of the interface profile to increase, and the adhesion will be improved after the UHPC overlay is poured and solidified. On the other hand, when the slant shear specimen is subjected to axial stress, the tangential force parallel to the interface and the normal
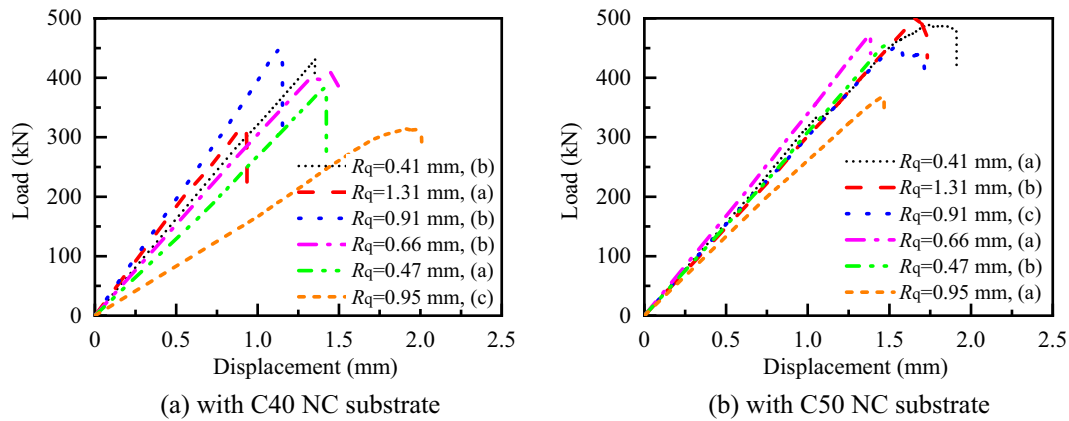

Fig. 5 Average load–displacement curves

Table 2 Bearing capacity of the tested samples (kN)

Substrate strength		R_q					
		0.41 mm	0.47 mm	0.66 mm	0.91 mm	0.95 mm	1.31 mm
C40	Sample 1	341.8	272.7	376.8	359.5	455.8	433.2
	Sample 2	287.9	360.5	529.9	450.5	534.6	615.6
	Sample 3	313.5	429.2	489.6	481.1	355.8	503.8
	Average	314.4	354.1	465.4	430.4	448.8	517.5
C50	Sample 1	389.6	430.5	515.5	597.8	458.9	531.1
	Sample 2	403.4	461.3	438.6	534.6	513.1	537.3
	Sample 3	287.9	375.3	525.4	403.7	548.8	523.1
	Average	360.30	422.35	493.12	512.05	506.96	530.50

Zhang *et al. Int J Concr Struct Mater* (2024) 18:18

Page 7 of 16
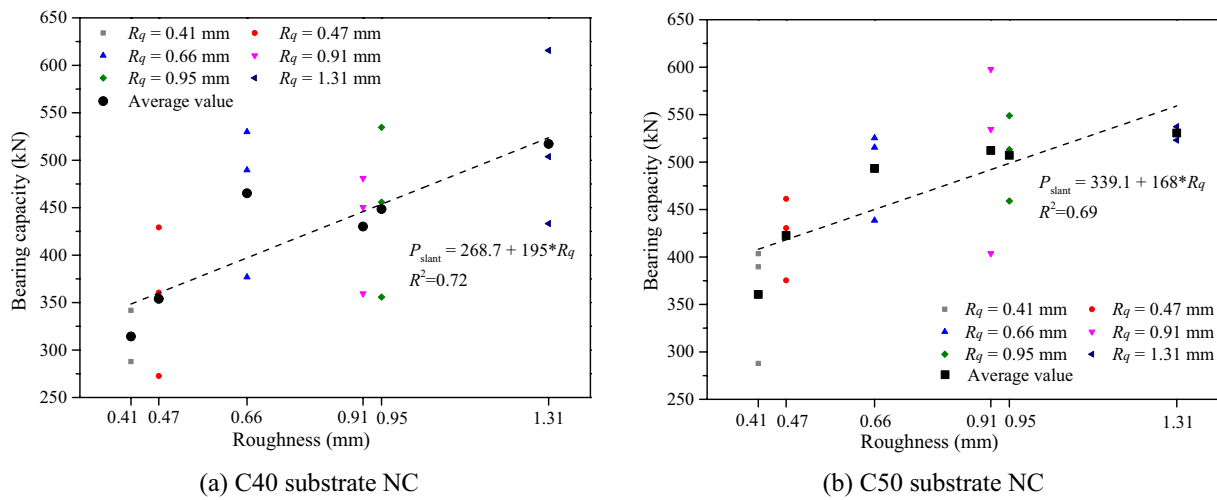

(a) C40 substrate NC

(b) C50 substrate NC

Fig. 6 Relationship between interface roughness and slant shear strength

stress perpendicular to the interface will be generated at the interface. Therefore, the increase in roughness will also increase the slant shear strength. For the shear plane with an included angle of 30°, the ratio of normal compressive stress to tangential shear stress borne by the interface is 1:1.73. The average shear capacity of specimens with C40 substrate and roughness $R_q = 0.41$ mm, 0.47 mm, 0.66 mm, 0.91 mm, 0.95 mm, and 1.31 mm is 314.4 kN, 354.1 kN, 465.4 kN, 430.4 kN, 448.8 kN, and 517.5 kN, respectively. When the interface roughness increases from 0.41 mm to 1.31 mm, the bearing capacity increases by 64.6% correspondingly, and the linear correlative coefficient is $R^2 = 0.72$. For specimens with C50 substrate, the average slant shear capacity is 360.3 kN, 422.4 kN, 493.1 kN, 512.0 kN, 506.9 kN, and 530.5 kN, respectively. Compared with the specimen with interface roughness of 0.41 mm, the slant shear capacity increases by 47.2% when the roughness is 1.31 mm, and the linear correlative coefficient is $R^2 = 0.69$. It can be calculated that when the substrate strength increases from C40 to C50, the shear strength increases by 14.6%, 19.3%, 5.9%, 19.0%, 13.0%, and 2.5%, respectively. This indicates that the strength of the substrate has been fully utilized, what's more, a stronger bonding behavior has been formed at the interface.

According to the failure modes displayed in Fig. 4, it can be seen that the failure modes of NC–UHPC slant shear specimens mainly include the interface debonding and the substrate concrete failure, and there are almost no obvious cracks appearing on the surface of the UHPC part. It is obvious in Fig. 7 that the rough interface is sheared at some UHPC bulge area; therefore, the UHPC bulges at the chiseling point can bear the shear force during the diagonal shear. To analyze

Fig. 7 Shear failure of UHPC bulge at the chisel point

the internal composition of the slant shear capacity, it is necessary to simplify and equivalent according to the test phenomena and results. In this research, it is assumed that the interface shear resistance consists of three parts: the shear resistance at the root of the chisel point, the shear bond force, and the shear friction force. In addition, based on the analysis of the failure process, it is also assumed that the bond strength of the interface is controlled by the tensile strength of the substrate concrete, and the shear strength at the root of the chisel point is controlled by the tensile strength of UHPC and the normal bond stress of the interface.

According to the research of Gopal (2020) and Yu (2022b), the interface slant shear strength V is composed of the uneven shear resistance (chisel root shear resistance) V_r, the interface bonding resistance V_c, and the interface friction resistance V_f:

Zhang *et al. Int J Concr Struct Mater*   (2024) 18:18

Page 8 of 16

$$V = V_r + V_c + V_f \tag{2}$$

The maximum principal tensile stress theory is used to calculate the shear resistance of the chisel point, and the feasibility of this method has been verified by many studies (Yu et al., 2022b). The calculation diagrammatic sketch is shown in Fig. 8, so the main tensile stress in the interface area can be calculated by the following formula:

$$\sigma_{11} = \frac{\sigma_x + \sigma_y}{2} + \sqrt{\left(\frac{\sigma_x + \sigma_y}{2}\right)^2 + \tau_{xy}^2}. \tag{3}$$

For the slant shear specimen, the interface bears the compressive stress $\sigma_x = \sigma_n$ and is taken as negative. In the ultimate state, there is $\sigma_{11} = f_t$, and f_t is the uniaxial tensile strength of UHPC; therefore, the ultimate shear stress τ_{xy} can be calculated as

$$\tau_{xy} = \sqrt{\left(f_t + \frac{\sigma_n}{2}\right)^2 - \left(\frac{\sigma_n}{2}\right)^2}. \tag{4}$$

Then, the shear bearing capacity of chisel points can be calculated by the following formula:

$$V_r = A_r \tau_{xy}, \tag{5}$$

where A_r is the area of the chisel point. Assuming that the chisel point is hemispherical, the part bearing the shear force is the root of the chisel point, and the shear area is the circular area with a diameter of L_r.

The shear bond resistance V_c is equal to the shear strength minus the contribution of UHPC shear resistance at the chisel point when the shear plane cannot be restrained. In this study, the interface unconstrained shear strength is taken as the double shear strength with the corresponding interface roughness, so there is

$$V_c = V_{bi} - V_r \tag{6}$$

where V_{bi} is the bi-surface shear strength. The friction resistance V_f of the interface is equal to the total shear component V of the slant interface shear strength minus the bi-surface shear strength of the corresponding roughness:

$$V_f = V - V_{bi} \tag{7}$$

For the SR and HR types of interface, they are both relatively flat; therefore, only shear bond resistance is considered. The calculated average chisel root shear resistance V_r, the interface bonding resistance V_c, and the interface friction resistance V_f of the specimen configured with different roughness and substrate strength are shown in Fig. 9. It can be seen that the shear resistance of slant shear is mainly composed of interface bonding resistance V_c and friction resistance V_f, and the root shear resistance V_r of chiseled point accounts for a very small part (less than 4%). For the slant shear specimens of C40 substrate concrete, the proportion of bond resistance is 29.6–78.4%, and the proportion of friction resistance is 21.6–67.0%. While for the C50 substrate configured specimen, the proportion of bond resistance and friction resistance is 40.1–78.7% and 21.3–56.7% respectively. In addition, with the increase of interface roughness, the proportion of bond shear resistance increases. This indicates that the increase in roughness will greatly improve the bonding property of the interface, thereby improving the resistance to shear failure.

3.3 Interfacial Slip Characteristics

The interface slip characteristics of the slant shear process are also very significant to evaluate the interface bond failure performance. The load–interface slip curves corresponding to the different substrate strength and interface roughness configurations are shown in Fig. 10. Taking the original position of the slip displacement (0 slip value) as the boundary, the slip curves of the two substrate strengths are symmetrically displayed on both sides. The slip curve is the average result of the interface slip collected from the two sides of the sample. Unlike the brittle failure characteristics shown in the load–displacement curve results, most NC–UHPC slant shear load–interface slip curves show a significant yield (ductility) stage, as shown in Fig. 10a. The load–interface slip curve can be divided into three stages: the elastic rising stage, the yielding stage, and the failure falling stage. Most of the experimental curves show the characteristics of the
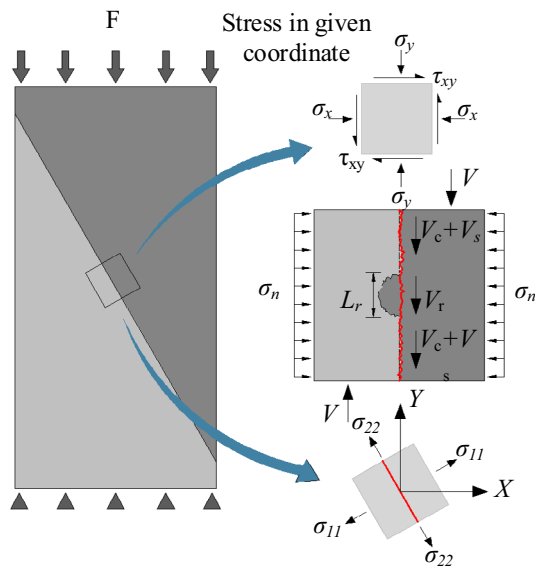

Fig. 8 Schematic diagram of the interface shear calculation

Zhang *et al. Int J Concr Struct Mater* (2024) 18:18
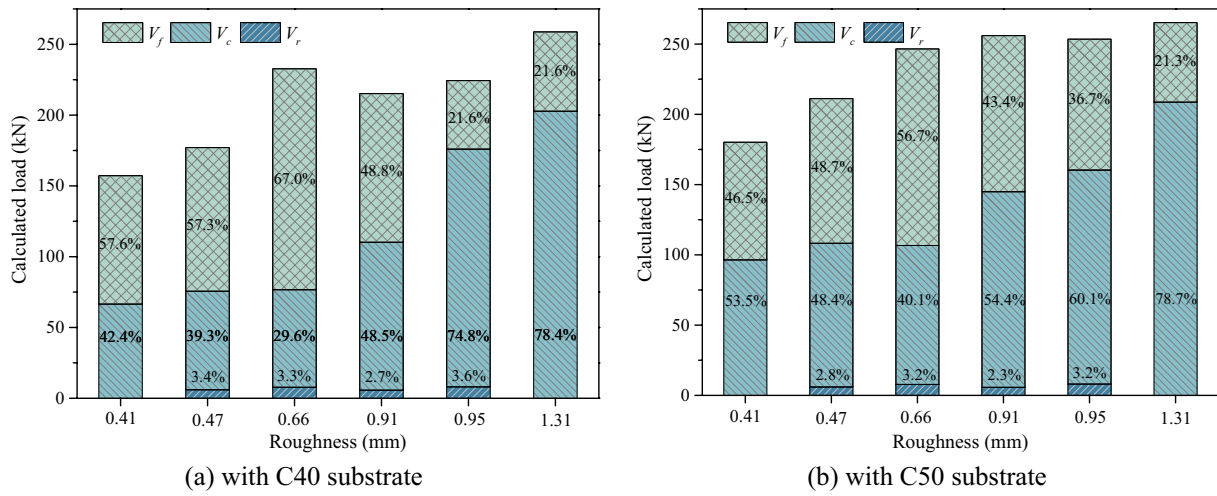
Page 9 of 16

Fig. 9 Shear resistance contribution of each part

"rising stage + yielding stage", and few load–interface slip displacement curves only show the elastic stage. Except for the obvious descending branch of the C50-2 sample in Fig. 10e, almost all of the curves have no obvious descending branch.

Compared with the load–displacement curves in Fig. 5, the load–interface slip curves show more obvious differences. The total compression deformation of the NC–UHPC specimen in the compression–shear process includes the elastic compression deformation, interface damage sliding of the UHPC part, and the compression cracking deformation of the NC part. The maximum slip displacement of the interface slip curves in Fig. 10 is 1.08 mm, while the vertical compression displacement reaches 2.61 mm. It can be seen that the final vertical deformation of the specimen is far greater than the slip displacement of the interface. The nonlinear failure of the interface shear process shows that the interface slip begins to increase after the initiation of the damage, and the nonlinear evolution of the slip curve occurs due to the shear resistance and mechanical interlocking effect. The load–displacement curves shown in Fig. 5 increase steadily before the shear failure, while the interface slip curve shows different evolution forms during loading. There is almost no interface slip at the low load level, when the load reaches 10–30% P_{max}, the interface slip starts to increase significantly. However, the corresponding load–displacement curve does not change significantly, the reason is that the interface slip value is too small relative to the loading displacement. As the load continues to increase, the relative slip at the interface increases rapidly. When the external load reaches the interface shear yield stress, it will cause the final failure of the slant shear specimen after superposition with the substrate damage.

Based on the analysis of the load–interface slip characteristics, the load is then normalized, and the interface slip values corresponding to the load ratio P/P_{max} of 0, 0.2, 0.4, 0.6, 0.8, and 1 are extracted, respectively. In addition, the average value is calculated from the copied specimen, and the results are shown in Fig. 11. Furthermore, the average interface slip difference between the C40 and C50 substrate specimens under the different load levels is calculated, respectively. The calculation results show that the variation trend of the average interface slip is consistent with the increase of the load level. At the lower load level, the growth rate of the interface slip is small, when the load reaches a higher level ($0.8P_{max} \sim P_{max}$), the interface slip indicates a significant growth change. For the different interface roughness configurations, the average slip displacement corresponding to the C40 substrate is almost greater than that of the C50 substrate specimen under the different load levels. This is mainly because the strength of the ITZ between the C40 substrate concrete and UHPC is weak, and the modulus of the substrate concrete with lower strength is smaller. While under the same load level, the shear slip deformation of the interface could be larger.
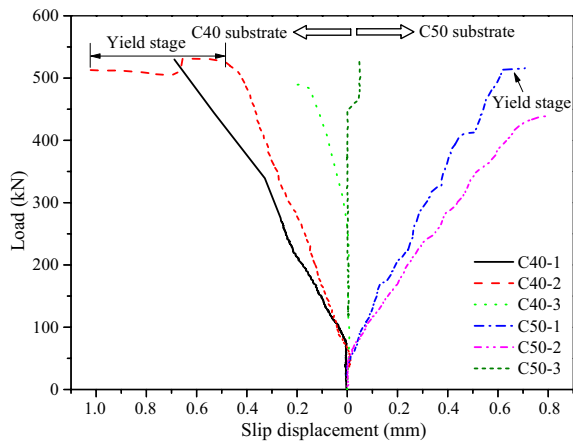
The interface average slip displacement difference (histogram) of C40 and C50 substrate samples under the different load levels in Fig. 11 shows that, before reaching the ultimate load level ($0 \sim 0.8P_{max}$), the average interface slip displacement difference of the two kinds of specimens increases with the increase of the load level. Compared with the slip displacement difference of $0.8P_{max}$, when reaching the ultimate load state, this interface slip difference decreases when the roughness is 0.47 mm, 0.91 mm, 0.95 mm, and 1.31 mm. As the interface roughness increases from 0.41 mm to 1.31
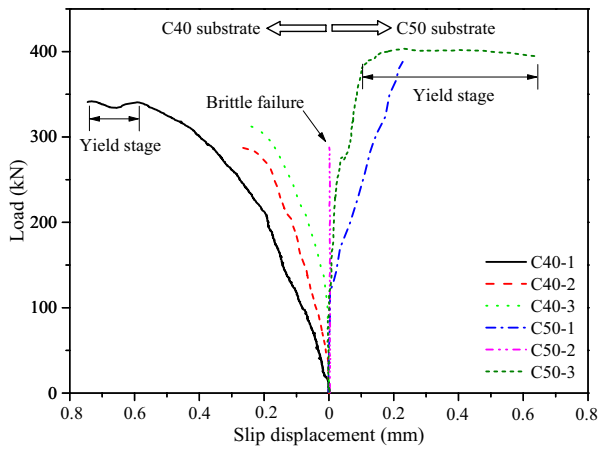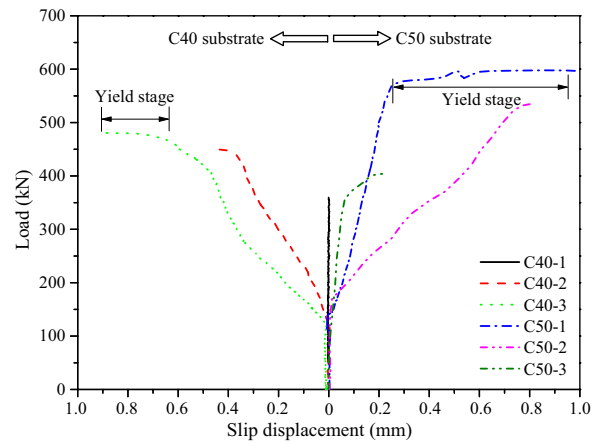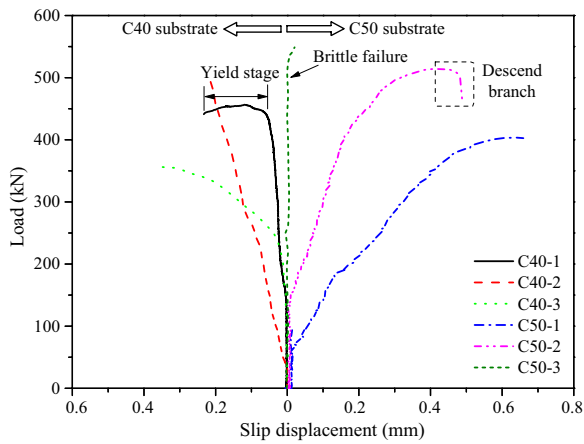
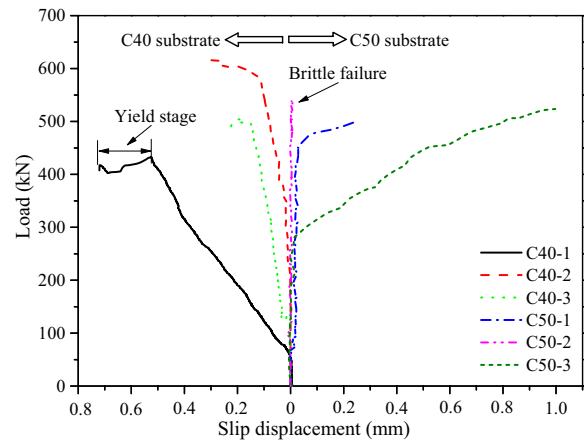(a) SR, $R_q = 0.41$ mm
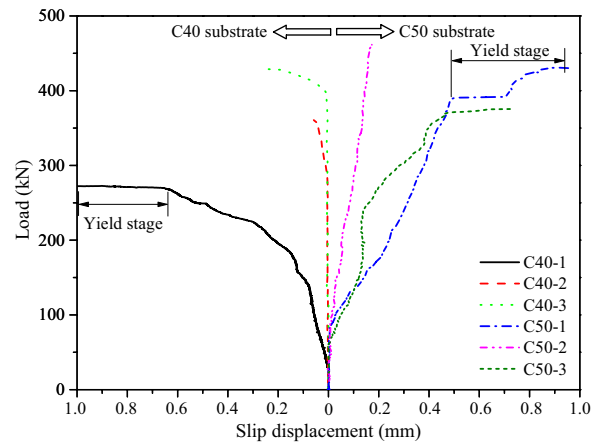
(b) CR-C4, $R_q = 0.47$ mm

(c) CR-C2, $R_q = 0.66$ mm

(d) PR, $R_q = 0.91$ mm

(e) CR-C6, $R_q = 0.95$ mm

(f) HR, $R_q = 1.31$ mm

Fig. 10 Load–interface slip curves of the slant shear test

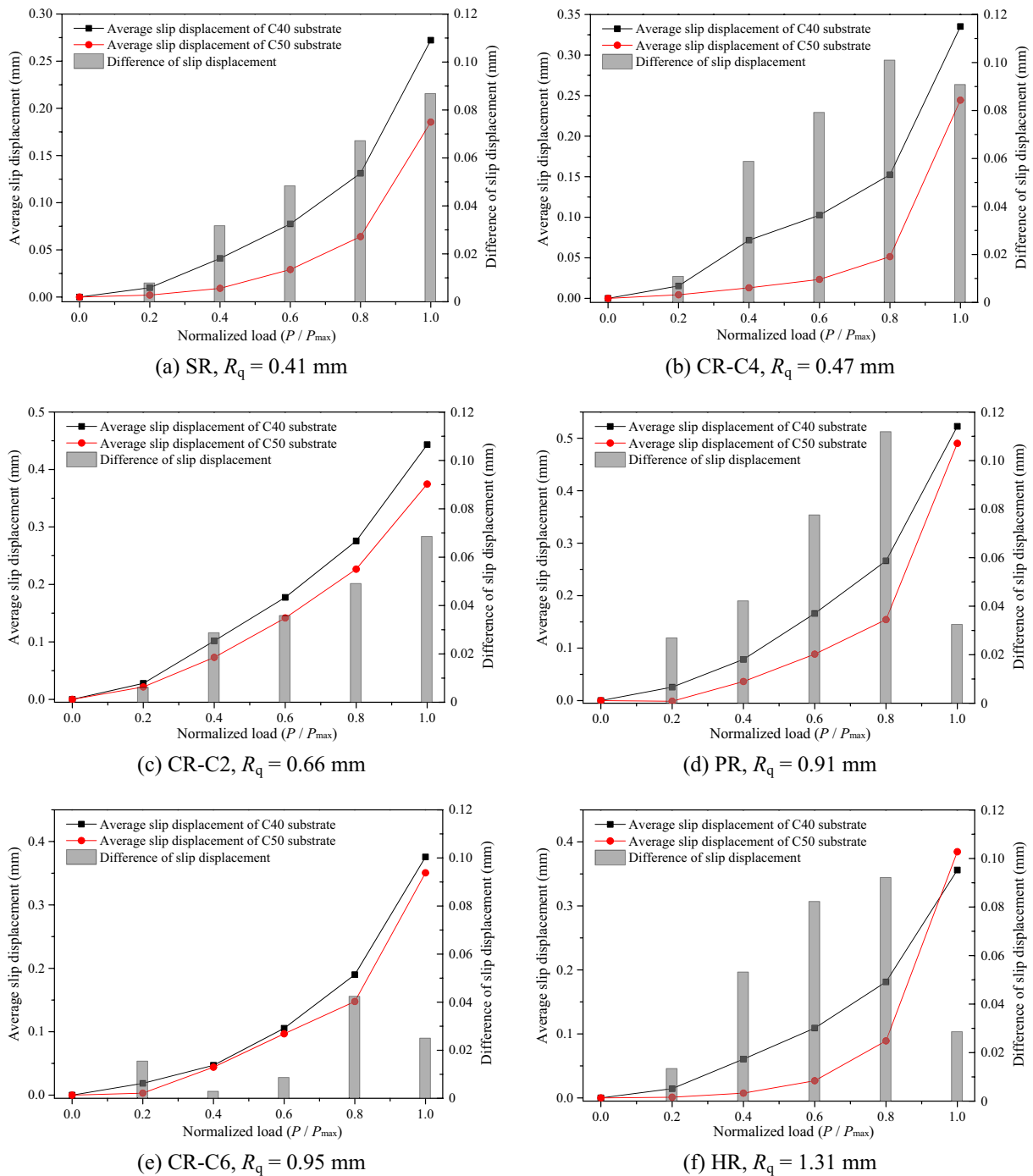Zhang *et al. Int J Concr Struct Mater*   (2024) 18:18

Page 11 of 16

Fig. 11 Load–interface slip curves of the slant shear test

mm, the maximum average slip displacement difference of C40 and C50 substrate slant shear specimens is 0.087 mm, 0.101 mm, 0.069 mm, 0.112 mm, 0.042 mm, and 0.092 mm, respectively, which is far less than the corresponding interface average slip displacement. The

results indicate that the change of substrate strength has little effect on the interface slip characteristics.

Based on the analysis of the interface average slip characteristics, the average maximum slip displacement corresponding to the different roughness is compared, and
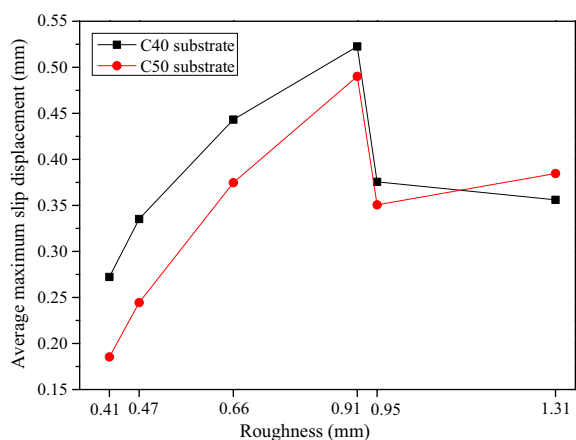
Fig. 12 Interface average maximum slip displacement under different roughness and substrate strength

the results are shown in Fig. 12. The results imply that with the increase of the roughness, the trend of the average maximum slip displacement of the two substrates specimens is consistent. With the different roughness configurations, the ultimate failure slip displacement of the C40 substrate specimen is greater than that of the C50 substrate specimen. When the interface changes from the relatively flat to the rough situation, the average maximum slip displacement of the interface increases first and then decreases, and the maximum slip occurs when the roughness $R_q = 0.91$ mm. The reason for this change is that when the interface roughness is small, as a result of the poor interface bonding property, the interface slip value of the final failure is small. With the increase of roughness, the interface maximum slip value increases continuously, while when the interface roughness exceeds 0.91 mm, the maximum slip value of the interface decreases rapidly. This is because when the roughness exceeds a certain value, the failure mode of the NC–UHPC slant shear specimen is not only limited to the interface failure but also occurs in the NC substrate with low strength. To ensure the effectiveness of UHPC in repairing concrete structures, reasonable rough interfaces should be considered.

3.4 Microstructure Properties of ITZ

The bond between the substrate and the overlay is considered to be the weakest part of the concrete repair system, which is similar to the interface between coarse aggregate and hardened cement paste in concrete. Therefore, the microstructure performance between the repair materials and the substrate concrete surface plays an intuitive and important role in the bonding behavior (Feng et al., 2022). The bonding force of the NC–UHPC interface includes the chemical bonding force at the micro-scale

and the mechanical interlocking force at the meso-scale. When the interface between the two materials does not slip under the shear load, the interface shear resistance consists of two parts. While if the microstructure of the interface is damaged and starts to slide, the chemical bonding force disappears, and the interface bonding interaction is only provided by the mechanical interlocking force or anchoring force of the rough surface.

To observe the microstructure of the interface between the substrate concrete and UHPC repair materials more intuitively, scanning electron microscopy (SEM) was used to observe the microstructure of the interface. The micro-scale scanning results can be used to assist in analyzing the macro-scale test results, which is also an effective way to reveal the shear failure mechanism between the substrate NC and UHPC. The microscopic scanning morphology of the interface under 77, 300, 1000, and 2000 times magnification was collected respectively, and the results are shown in Fig. 13. It can be seen from Fig. 13a that the ITZ displayed at 77 magnification is not so obvious, and the NC substrate is closely combined with UHPC. There are obvious spherical pores on the side of the NC substrate and unconnected micro-cracks near ITZ. The 300 times microscopic morphology is shown in Fig. 13b. It is found that the width of ITZ is mostly 50–100 μm, and because of the inherent loose microstructure characteristics of ITZ, the existence of micro-cracks can be observed in this area. After the ITZ is magnified 1000 and 2000 times, respectively (Fig. 13c and d), the loose flaky crystalline structure of ITZ is clearly displayed. Although there is an obvious strength difference between the NC substrate and UHPC, the properties of hydration products generated after the hydration reaction are basically the same. During the UHPC curing process, some water in the UHPC mortar will be absorbed by the surface of the substrate concrete. The reduction of water will reduce the degree of hydration reaction of UHPC near the interface area, which could cause the insufficient hydration reaction of cement particles, and further give rise to the ITZ microstructure being mainly composed of lamellar $Ca(OH)_2$ crystals.

Fig. 14 shows the microstructure morphology of the ITZ area with 2440 and 20,000 times magnification. After pouring UHPC at the NC substrate, due to the influence of evaporation and migration of moisture at the interface, there will be a seepage layer from the substrate concrete to the UHPC side. This area mainly exists on the side of the NC substrate while near the interface, which is the secondary hydration production mainly composed of active powder without hydration or incomplete hydration in the substrate concrete. The main components are Calcium Silicate Hydrate (C–S–H) gel, a small amount of Ettringite crystal (AFt), and $Ca(OH)_2$ crystal (CH). At the

Zhang *et al. Int J Concr Struct Mater*   (2024) 18:18
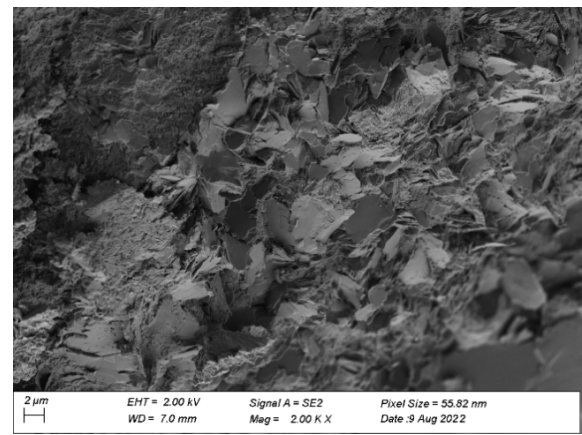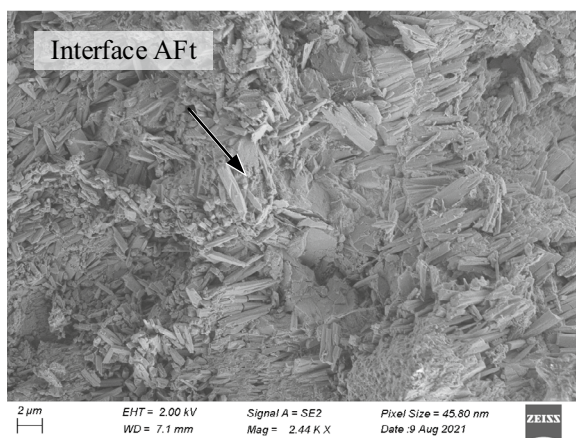
Page 13 of 16
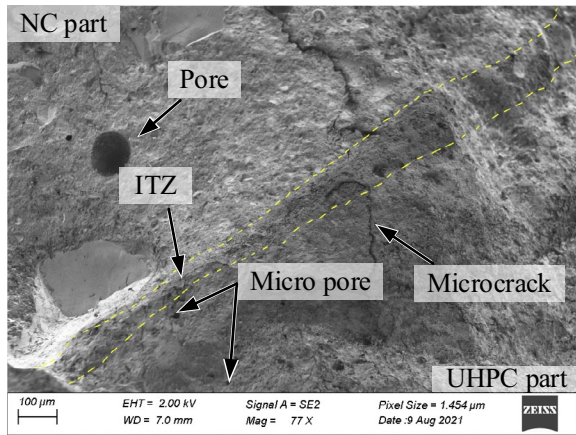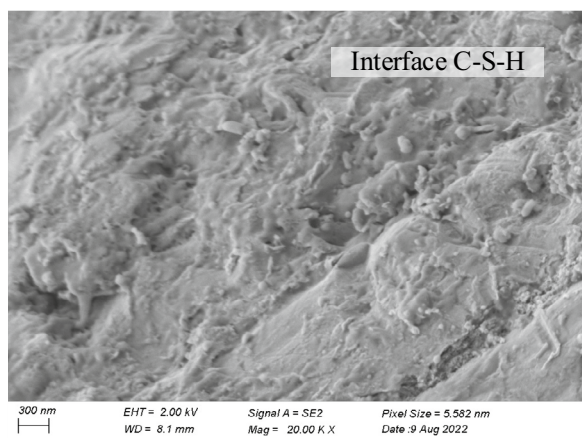

(a) 77 times
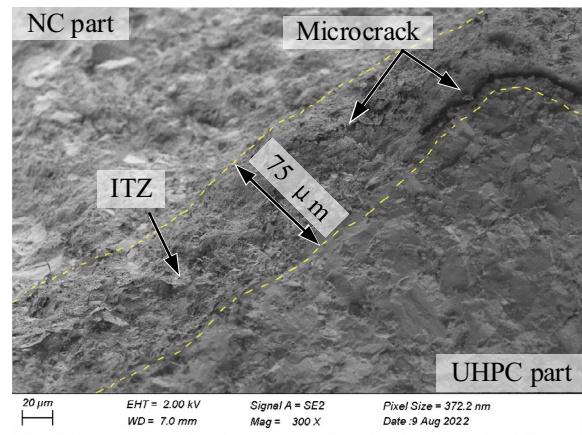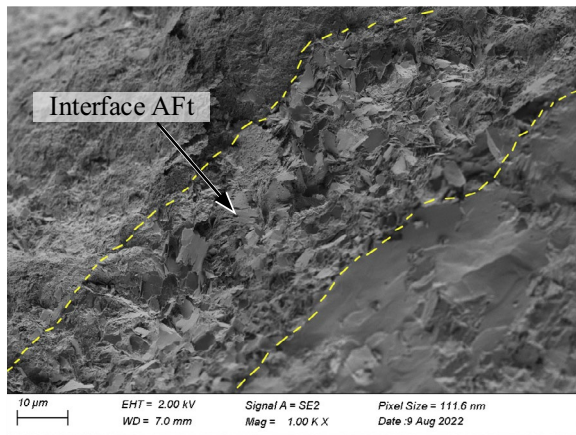
(b) 300 times

(c) 1000 times

(d) 2000 times

Fig. 13 Different magnification SEM images of the ITZ between NC and UHPC

(a) 2440 times

(b) 20000 times
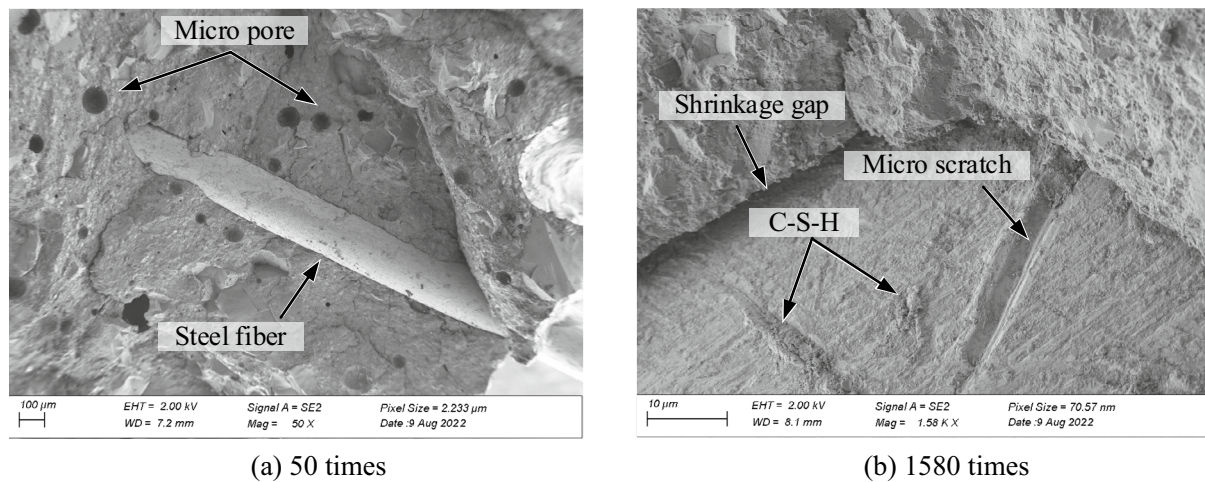
Fig. 14 Micro-scale hydration morphology of C–S–H

Zhang *et al. Int J Concr Struct Mater*   (2024) 18:18

Page 14 of 16

(a) 50 times

(b) 1580 times

Fig. 15 Micromorphology of fibers in UHPC matrix

same time, the active ions existing in the UHPC cement matrix will react with the substrate cement particles to generate the flocculent C–S–H products to fill the micro-voids and micro-cracks (Fig. 14b), which enhances the bonding performance between the repair materials and the base surface and extends to the hardened layer of the substrate concrete. While the ITZ main layer consisting of needle-like AFt crystals and CH is next to the penetration layer, which greatly reduces the bonding strength. In this transition area, the microscopic particles of silica fume that are not fully reacted in the post-poured UHPC react with $Ca(OH)_2$ to form the micro C–S–H crystals. The larger specific surface area increases the van der Waals force between the tiny calcium silicate crystals. With the increase in the number of tiny crystals, the ITZ has a larger specific surface area, which can improve the bonding performance of ITZ. However, AFt crystals with unstable microstructures and needle-like CH crystals form a large number of loose fragile microstructures, which greatly reduce the strength of the region and become the key factor to determine the macro-bonding performance. The ITZ near the UHPC side has a microstructure similar to that of UHPC, and the bonding property of this area is obviously better than that of the interlayer. The water/cement ratio of UHPC and the characteristics of powder materials have a direct impact on this area.

The SEM results of steel fiber in the UHPC matrix are shown in Fig. 15. In the SEM results at 50 times magnification (Fig. 15a), the steel fibers are well-embedded in the UHPC matrix. In the curing process, the moisture near the steel fiber will move toward them due to the inherent hydrophilicity of the steel fiber. This process increases the water/cement ratio near the steel fiber and intensifies the hydration near the steel fiber, and further improves the bond between the steel fiber and the matrix. During the solidification process, the drying shrinkage of the matrix near the steel fiber will also increase correspondingly, which will make the steel fiber subject to greater normal pressure, and tightly wrapped by the matrix. The greater restraint force makes the friction between the steel fiber and the matrix increase, which greatly improves the toughening effect of the fiber. As shown in Fig. 15b, the 1580 times magnification SEM results indicate that there is a micro-gap between the steel fiber and the matrix. This is mainly due to the higher water/cement ratio near the steel fiber, which leads to the increase in shrinkage of the UHPC matrix. On the surface of the steel fiber, the micro-scratches produced during the mixing process can also be observed. Such micro-scratches and hydrated C–S–H productions on the fiber surface lead to a great increase in the surface roughness of the steel fiber, which increases the friction effect when the fiber is pulled out. Based on strengthening the mechanical anchoring effect of the bonding interface, the repair and reinforcement effect of UHPC on the damaged NC structures will be greatly improved.

4 Conclusions

Based on the slant shear tests and SEM tests, the shear failure behavior of the NC–UHPC interface was investigated, revealing the shear failure mechanism as well as influence of the substrate strength and the interface roughness. The following conclusions can be drawn:

(1) The NC–UHPC interface could gain satisfied bond performance under compression–shear loading. The NC substrate and UHPC overlay are con-

formed to be tightly combined at the interface transition zone (ITZ) by the SEM test, and the measured interfacial shear strength reaches 19.4 MPa with C40 substrate and 21.8 MPa with C50 substrate.

(2) The width of the ITZ is around 50–100 μm. The Calcium Silicate Hydrate (C–S–H) gel, the Ettringite crystal (AFt), and the $Ca(OH)_2$ crystal (CH) form its loose microstructure. The van der Waals force between the tiny calcium silicate crystals could be enhanced by the large specific surface area of the flocculent C–S–H products, resulting in improved bonding performance of the ITZ.

(3) The slant shear resistance is mainly provided by the chisel point root, the interface bond, and the friction. With the increase of interface roughness, the proportion of the interfacial bond resistance increases.

(4) Brittle interfacial failure have been observed, and the failure modes include (a) interface debonding failure, (b) interface debonding+substrate cracking, and (c) interface failure+substrate crushing failure. As the interface roughness rises, the prone failure mode changes from mode (a) to mode (c). As the substrate strength rises, the prone failure mode changes from mode (c) to mode (a) and (b).

(5) Both the higher interface roughness and the higher substrate strength have positive effect on the slant shear resistance of the ITZ. When the roughness increases from $R_q=0.41$ mm to $R_q=1.31$ mm, the corresponding slant shear resistance increases by 64.6% and 47.2% with C40 and C50 substrate, respectively. When the substrate strength increases from C40 to C50, the slant shear resistance can be increased by 19.3% with $R_q=0.47$ mm.

(6) The normalized load–interface slip relationship indicates that the slip value of a specimen is higher with C40 substrate than that with C50 substrate, and the differences go up with in $0 \sim 0.8P_{max}$.

References
Aaleti, S., & Sritharan, S. (2019). Quantifying bonding characteristics between UHPC and normal-strength concrete for bridge deck application. *Journal of Bridge Engineering, 24*, 04019041.

Al Hallaq, A., Tayeh, B. A., Shihada, S. (2017). Investigation of the bond strength between existing concrete substrate and UHPC as a repair material. *International Journal of Engineering and Advanced Technology (IJEAT)*, 6.

Bentz, D. P., De la Varga, I., Munoz, J. F., Spragg, R. P., Graybeal, B. A., Hussey, D. S., et al. (2018). Influence of substrate moisture state and roughness on interface microstructure and bond strength: slant shear vs pull-off testing. *Cement and Concrete Composites, 87*, 63–72.

Carbonell Muñoz, M. A., Harris, D. K., Ahlborn, T. M., & Froster, D. C. (2014). Bond performance between ultrahigh-performance concrete and normal-strength concrete. *Journal of Materials in Civil Engineering, 26*, 04014031.

Ekaputri, J. J., Indriyantho, B. R., Han, A., & Gan, B. S. (2022). Shear-bond behavior of self-compacting geopolymer concrete to conventional concrete. *Construction and Building Materials, 321*, 126167.

Feng, S., Xiao, H. G., Liu, R., Liu, M. (2022). The bond properties between ultra-high-performance concrete and normal strength concrete substrate: Bond macro-performance and overlay transition zone microstructure. *Cement and Concrete Composites, 128*, 104436. https://doi.org/10.1016/j.cemconcomp.2022.104436.

Feng, S., Xiao, H., & Li, H. (2020). Comparative studies of the effect of ultrahigh-performance concrete and normal concrete as repair materials on interfacial bond properties and microstructure. *Engineering Structures, 222*, 111122.

Feng, S., Xiao, H., Liu, R., & Liu, M. (2022). The bond properties between ultra-high-performance concrete and normal strength concrete substrate: Bond macro-performance and overlay transition zone microstructure. *Cement and Concrete Composites, 128*, 104436.

Gopal, B. A., Hejazi, F., Hafezolghorani, M., & Voo, Y. L. (2020). Shear strength of dry and epoxy joints for ultra-high-performance fiber-reinforced concrete. *ACI Structural Journal, 117*, 279–288.

Harris, D. K., Munoz, M. A. C., Gheitasi, A., Ahlborn, T. M., & Rush, S. V. (2014). The challenges related to interface bond characterization of ultra-high-performance concrete with implications for bridge rehabilitation practices. *Advances in Civil Engineering Materials, 4*, 75–101.

Hu, B., Li, Y., & Liu, Y. (2020). Dynamic slant shear bond behavior between new and old concrete. *Construction and Building Materials*. https://doi.org/10.1016/j.conbuildmat.2019.117779

Huang, Y., Grünewald, S., Schlangen, E., & Luković, M. (2022). Strengthening of concrete structures with ultra high performance fiber reinforced concrete (UHPFRC): A critical review. *Construction and Building Materials, 336*, 127398.

Jafarinejad, S., Rabiee, A., & Shekarchi, M. (2019). Experimental investigation on the bond strength between ultra high strength fiber reinforced cementitious mortar & conventional concrete. *Construction and Building Materials, 229*, 116814.

Zhang *et al. Int J Concr Struct Mater*   (2024) 18:18

Page 16 of 16

Paschalis, S. A., & Lampropoulos, A. P. (2021). Developments in the use of ultra high performance fiber reinforced concrete as strengthening material. *Engineering Structures, 233*, 111914.

Valikhani, A., Jahromi, A. J., Mantawy, I. M., & Azizinamini, A. (2020). Experimental evaluation of concrete-to-UHPC bond strength with correlation to surface roughness for repair application. *Construction and Building Materials, 238*, 117753.

Yang, H., Zheng, Y., Mo, S., & Lin, P. (2022). Push-out tests on studs with UHPC cover embedded in UHPC-NSC composite slab. *Construction and Building Materials, 331*, 127210.

Yu, J., Zhang, B., Chen, W., & He, J. (2020). Experimental and multi-scale numerical investigation of ultra-high performance fiber reinforced concrete (UHPFRC) with different coarse aggregate content and fiber volume fraction. *Construction and Building Materials, 260*, 120444.

Yu, J., Zhang, B., Chen, W., & Liu, H. (2022a). Multi-scale analysis on the tensile properties of UHPC considering fiber orientation. *Composite Structures, 280*, 114835.

Yu, K., Zhang, Z., Zou, Y., Jiang, J., Zeng, X., & Tang, L. (2022b). Interfacial shear performance of epoxy adhesive joints of prefabricated elements made of ultra-high-performance concrete. *Polymers, 14*, 1364.

Zanotti, C., & Randl, N. (2019). Are concrete-concrete bond tests comparable? *Cement and Concrete Composites, 99*, 80–88.

Zanotti, C., Rostagno, G., & Tingley, B. (2018). Further evidence of interfacial adhesive bond strength enhancement through fiber reinforcement in repairs. *Construction and Building Materials, 160*, 775–785.

Zhang, Y., Chen, Q., Wang, Z., Zhang, J., Wang, Z., & Li, Z. (2019). 3D mesoscale fracture analysis of concrete under complex loading. *Engineering Fracture Mechanics, 220*, 106646.

Zhang, Y., Huang, S., Zhu, Y., Hussein, H. H., & Shao, X. (2022). Experimental validation of damaged reinforced concrete beam strengthened by pretensioned prestressed ultra-high-performance concrete layer. *Engineering Structures, 260*, 114251.

Zhang, Y., Zhu, P., Liao, Z., & Wang, L. (2020). Interfacial bond properties between normal strength concrete substrate and ultra-high performance concrete as a repair material. *Construction and Building Materials, 235*, 117431.

Publisher's Note

Boshan Zhang   Assistant Professor in Department of Bridge Engineering, Tongji University, Shanghai, China.

Jiangjiang Yu   PhD candidate in Department of Building and Real Estate, Hong Kong Polytechnic University, Hong Kong, China

Weizhen Chen   Professor in Department of Bridge Engineering, Tongji University, Shanghai, China.

Jianbo Chen   Staff in Highway Development Center of Hekou District, Dongying, China

Heng Li   Professor in Department of Building and Real Estate, Hong Kong Polytechnic University, Hong Kong, China.

Jialun Niu   Post-doctor in Department of Geotechnical Engineering, Tongji University, Shanghai, China.